Identification and Removal of Reaction Wheel Interference from In-Situ Magnetic Field Data using Multichannel Singular Spectrum Analysis

Matthew G. Finley[1], Robert M. Broadfoot[1], Sapna Shekhar[1], and David M. Miles[1]

[1]Department of Physics and Astronomy, University of Iowa, Iowa City, IA 52242, USA

Key Points:

- In-situ magnetic field measurements are often degraded by stray magnetic fields from the host spacecraft, such as from reaction wheels
- Decomposing magnetic field data from multiple sensors simultaneously using M-SSA allows separation of geophysical fields and local noise
- Automated component selection procedure allows for robust estimation and subtraction of local magnetic noise, improving data quality

Corresponding author: Matthew G. Finley, matthew-g-finley@uiowa.edu

Abstract

In-situ magnetic field measurements are critical to our understanding of a variety of space physics phenomena including field-aligned currents and plasma waves. Unfortunately, high-fidelity magnetometer measurements are often degraded by stray magnetic fields from the host spacecraft, its subsystems, and other instruments. One dominant source of magnetic interference on many missions are reaction wheels – spinning platters of varying rates used to control spacecraft attitude. This manuscript presents a novel approach to the mitigation of reaction wheel interference on magnetometer measurements aboard spacecraft where multiple magnetometer sensors are deployed. Specifically, multichannel singular spectrum analysis is employed to decompose multiple time series simultaneously. A technique for automatic component selection is proposed that classifies the decomposed signals into common geophysical signals and disparate locally generated signals enabling the robust estimation and removal of the local interference without requiring any assumptions about its characteristics or source. The utility of this proposed method is demonstrated empirically using in-situ data from the CASSIOPE/Swarm-Echo mission, and a data interval with near-constant background field was shown to have its local reaction wheel interference reduced from 1.90 nT RMS, for the uncorrected outboard sensor, to 0.21 nT RMS (an 89.0% reduction). This technique can be generalized to arrays of more than two sensors, and should apply to additional types of magnetic interference.

Plain Language Summary

Earth's magnetic fields are dynamic, and their interactions with solar wind may lead to the excitation of different types of currents and waves. In order to observe and study these processes, high-quality magnetic field measurements are necessary. However, the spacecraft carrying magnetic field sensors are often magnetically noisy – they produce stray magnetic fields that contaminate the measurements. One dominant noise source on many spacecraft are the systems that control the orientation of the spacecraft. This manuscript presents a novel approach to the suppression of magnetic interference caused by these systems, improving the quality of acquired data. Specifically, a technique for the simultaneous separation of multiple measurements into physically meaningful components is combined with an automated component selection technique. This allows for a high-quality estimate of the spacecraft noise to be generated and subsequently removed from magnetic field measurements, greatly improving the data quality. For example, an inter-

val of data captured by the CASSIOPE/Swarm-Echo satellite was shown to have its local interference reduced by an average of 89%.

1 Introduction

In-situ magnetic field measurements are used in heliophysics to sense the plasma waves and field-aligned currents that couple energy, mass, and momentum through near-Earth space. The geophysical fields being measured are typically composed of the quasi-static Earth field, quasi-sinusoidal signatures of wave processes, and field generated by current systems. While the wave speeds are typically fast compared to the speed of the spacecraft, the apparent field of the quasi-static Earth field and quasi-static current systems are strongly doppler-shifted by the spacecraft motion, causing them to appear strongly time-varying to an in-situ sensor. In practice, these measurements are often contaminated by stray magnetic fields generated by the host spacecraft, its subsystems, and other instruments (Miles et al., 2019). These stray fields can have magnitude as large—or larger—than the geophysical signals of interest and have significant overlap in the frequency domain, making them problematic to isolate. Quasi-DC effects caused by sources such as permanently magnetized materials and solar panel or battery currents can typically be removed through careful calibration, but more time-varying signals are typically much more difficult to remove.

In order to mitigate the impact of these interfering stray fields, magnetic field sensors are typically deployed on booms in order to move them away from the spacecraft. This physical separation moves the sensor away from the stray magnetic fields that are unavoidably generated by spacecraft subsystems. Spacecraft missions vary in both their magnetic cleanliness requirements and magnetometer boom lengths. Historical missions (e.g., Acuña et al. (1978)) have flown booms of five to ten meters. However, there are now many examples of spacecraft with increasingly short booms: Magnetospheric Multiscale (MMS) used 5-meter booms (Russell et al., 2016); Van Allen Probes used 3-meter booms (Kletzing et al., 2013); Space Technology 5 (ST-5) used 1.1-meter booms (Slavin et al., 2008); Dellingr used a 0.52-meter boom (Kepko et al., 2017); and Ex-Alta 1 used a 0.6-meter boom (Mann et al., 2020). Additionally, the upcoming Escapade mission plans to employ a 0.9-meter boom, and the upcoming TRACERS mission currently calls for a 1.1-meter boom. Although these shorter booms are cost-effective and convenient, they

provide less interference mitigation and can place the magnetometer sensor in the complex multi-pole near-field of the stray magnetic field.

A dual-sensor gradiometer of two magnetometer sensors is another well-established interference mitigation technique in space-based magnetic field measurements (Ness et al., 1971; Neubauer, 1975) Both sensors experience a common geophysical magnetic field, but the interfering stray field from the spacecraft drops of with distance and will be experienced at different intensities based on the distance between the sensors. In the simplest case, the difference in the measurements between the two sensors (ΔB) can be fit to a model of a static dipole-like magnetic field and subtracted to estimate the uncontaminated geophysical field. However, real-world stray fields that are time-varying and have non-trivial multipole harmonics are more challenging to remove. Historical model driven algorithms (Ness et al., 1971) generalize to multipole sources; however, this requires pre-launch characterization of the multipole stray field from the complete, integrated, and operating spacecraft. This characterization can be technically challenging or impossible due to the extreme local magnetic noise in most spacecraft vehicle assembly facilities. As a result, several interference mitigation techniques have been proposed that utilize advanced signal processing techniques—such as adaptive noise cancelation and independent component analysis—to identify magnetic interference from the host spacecraft without making assumptions about the signal structure or source (Pope et al., 2011; Sheinker & Moldwin, 2016; Imajo et al., 2021).

This work focuses primarily on interfering fields generated by so-called *reaction wheels*, which are spinning platters used to control the spacecraft orientation via momentum conservation. These wheels can create magnetic signatures both through the current used to sustain and vary their spin rates, and by the physical rotation of ferromagnetic materials used in their construction. This leads to interference composed of a variable-frequency sinusoid caused by the spin associated with each reaction wheel and the corresponding higher-order harmonics. The spin rates are reasonably constant when the satellite is flying straight-and-level but can change rapidly when the spacecraft maneuvers, making them difficult to remove via traditional bandpass filtering.

The primary source of data studied in this manuscript was captured by the Magnetic Field Instrument (Wallis et al., 2015) on the Enhanced Polar Outflow Probe (e-POP) aboard the CASSIOPE spacecraft (Yau & James, 2015), which is now operating

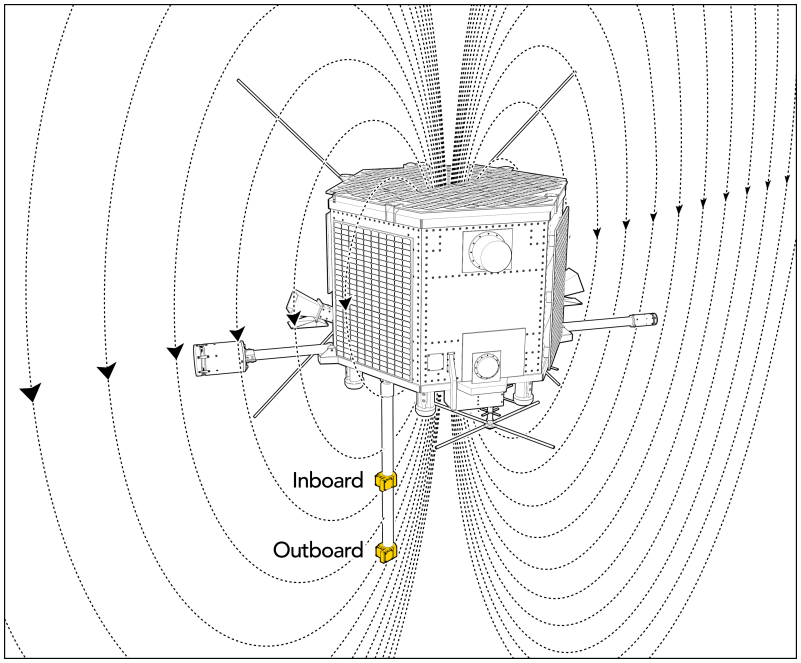

Figure 1: Illustration of the physical separation and orientation of the MGF inboard and outboard magnetometers on the CASSIOPE/Swarm-Echo spacecraft. Stray magnetic fields from the spacecraft, illustrated here as a simple dipole, drop off with distance and are experienced at different intensities by the two sensors.

as Swarm-Echo; part of the Swarm constellation in the European Space Agency Third Party Mission Program. Swarm-Echo is a low-cost multi-instrument small satellite studying plasma dynamics and radio propagation in the auroral ionosphere. The spacecraft carries a gradiometer of two identical fluxgate magnetometers deployed at different distances from the along a common 0.9-meter boom. This experiment was intended to enable studies of small-scale auroral processes and plasma waves, so the instruments are synchronized and each samples the local magnetic vector at 160 samples per second. Figure 1, adapted from Sen Gupta and Miles (2022), illustrates the two sensors. The mission had limited opportunities for a detailed magnetic cleanliness screening and hence both instruments encounter significant magnetic interference. Specifically, the e-POP/Swarm-Echo magnetic field data appears to be contaminated with stray field from three primary sources: quasi-static fields generated by ferromagnetic materials onboard the spacecraft; quasi-sinusoidal field generated by the spacecraft's reaction wheels; and time-varying field generated by spacecraft subsystem currents. The quasi-static fields are most easily re-

moved by in-situ calibration (e.g., Broadfoot et al. (2022)) and are not discussed throughout the remainder of this manuscript. Instead, this manuscript is focused on the removal of the quasi-sinusoidal reaction wheel signals, since they are a constantly-present feature inherent to the spacecraft's operation. Removal of this quasi-sinusoidal magnetic contamination will enable science utilization of the full-cadence data and future work investigating and mitigating other time-varying interference signals that are currently masked by the reaction wheel tone.

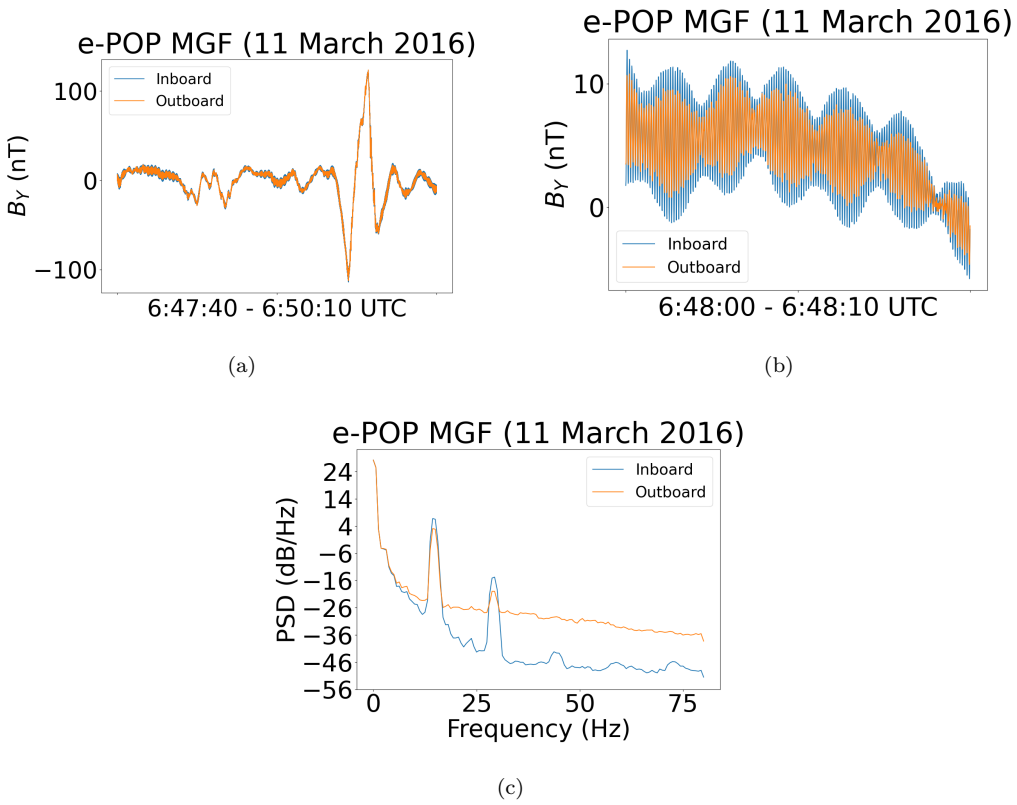

Figure 2: Magnetic field data captured by MGF on March 11, 2016 between 6:47:40 and 6:50:10 UTC. (a) Inboard and outboard measurements for the entire time period; (b) Ten-second sample that better illustrates the oscillatory reaction wheel interference; (c) Power spectral density for the inboard and outboard sensors.

Figure 2 provides an example of the data captured by Swarm-Echo's Magnetic Field Instrument (MGF). Figure 2a shows time-series data for the inboard and outboard sensors during a 150-second interval. Fig. 2b provides a ten-second sample of the total interval, illustrating the differences between inboard and outboard sensor measurements

and the dominant oscillatory reaction wheel interference. The spacecraft reaction wheels manifest in each sensor component as the sum of high-frequency sinusoids corresponding to the spin rate of each wheel - in this case approximately 15 Hz, with associated harmonics. As expected, the magnetic interference on the inboard sensor—which is closer to the spacecraft's reaction wheels—is larger than the interference experienced by the outboard sensor. Figure 2c provides the power spectral density for the inboard and outboard sensors during the time period shown in Fig. 2a. It can be seen that although the general trends of the reaction wheel harmonics are similar for the two sensors, there is a distinct nonlinear relationship between them in the frequency domain. This means that, as discussed previously, the complex multi-pole harmonics present make it difficult to remove higher-order harmonics by simply taking the difference of the two sensors (ΔB) and fitting it to a static dipole magnetic field.

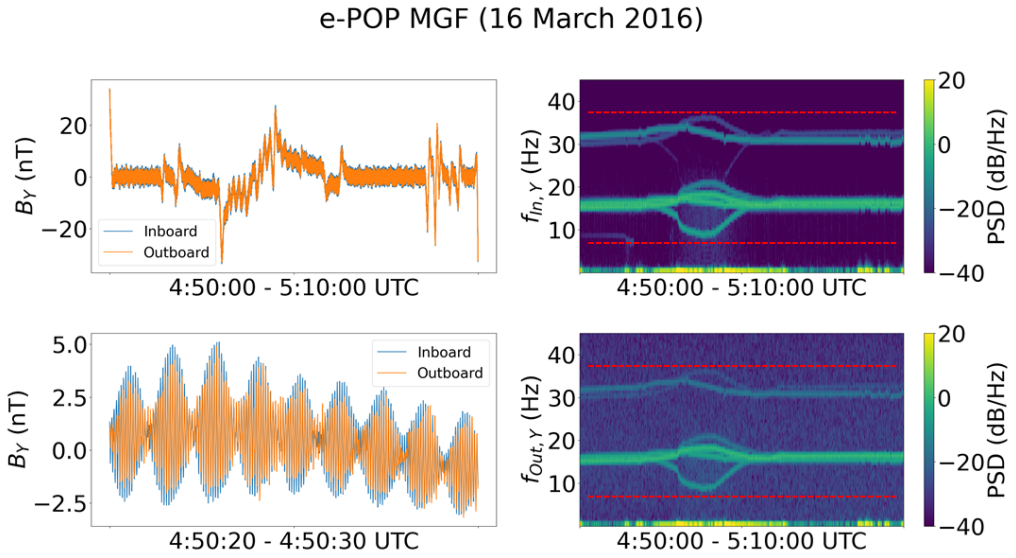

Figure 3: Magnetic field data captured by the MGF aboard e-POP on March 16, 2016 between 4:50:00 and 5:10:00 UTC. (left) Time series data associated with the entire interval and a zoomed view of the interval; (right) Spectrograms for both inboard and outboard magnetometers during the interval, with dashed red lines illustrating the approximate bandwidth associated with the reaction wheel interference as the wheel rates vary over time.

Swarm-Echo nominally maintains three-axis stabilized nadir-pointing attitude. However, slew-to-target maneuvers are used periodically to support different types of scien-

tific data acquisition such as auroral imaging. The spacecraft attitude control system has a nominal targeted rate for all wheels, originally at ∼15Hz, and will momentum dump between the wheels to maintain this. Figure 3 (left) shows a representative time series, for each MGF sensor, of the resulting magnetometer measurements during such a maneuver. Translating to the frequency domain (Fig. 3, right) shows the complex features generated for the inboard and outboard sensors as the wheel rates diverge from nominal during maneuvers and then are momentum dumped back to a common frequency. The dashed red lines illustrate the bandwidth in which the wheel rates dominate for this 20-minute time period. It can be seen that applying a bandpass filter to mitigate the reaction wheel interference would remove a huge frequency range, including the frequency bands in which geophysical signals of interest often manifest. More reasonable bandpass filters can be applied to the magnetic field measurements in order to avoid removing such a large frequency band, but will result in signals contaminated by reaction wheel interference when the wheel rates diverge from their nominal range.

In this manuscript, a novel method for the automatic suppression of magnetic interference caused by spacecraft reaction wheels in gradiometric magnetometer measurements is proposed. Specifically, multichannel singular spectrum analysis is utilized in order to simultaneously decompose the inboard and outboard measurements, and an automatic component selection algorithm is described that allows for the development of a robust estimate for the reaction wheel interference. This interference can subsequently be removed from the time-series measurements, enabling greater fidelity in the recovered data without the need for hand-tuned bandpass filters applied on a case-by-case basis.

2 Methodology

This section provides an overview of the analysis techniques used to isolate signals assumed to contribute to the magnetic interference caused by spacecraft reaction wheels. Applying these techniques to each of the three components of the vector magnetic field measurements allows the interference signal to be directly removed from the time-series magnetometer readings, improving fidelity and increasing the potential for meaningful analysis.

2.1 Singular Spectrum Analysis

Singular spectrum analysis (SSA) is a tool used to decompose a single time series into statistically meaningful components. Functionally, the algorithm performs singular value decomposition (SVD) on a trajectory matrix generated with columns as delayed copies of the original signal, enabling the eigenvectors and associated eigenvalues for the delay-space to be extracted (Broomhead & King, 1986; Vautard & Ghil, 1989). The eigenvalues can be used in order to determine which principal components (generated by projecting the eigenvectors onto the trajectory matrix) contain the largest variance in the system, which can be useful when attempting to isolate highly contributory signal components. Further, each of the principal components can be transformed into a time series with the same length as the original input signal. Thus, the original input signal is effectively decomposed into a set of statistically meaningful time series that, when summed together, fully reconstruct the input.

This technique has seen application in a wide range of fields such as geodynamics (Chen et al., 2013), climatology (Vautard & Ghil, 1989), and economics (Hassani & Zhigljavsky, 2009). However, this manuscript aims to identify and remove magnetic interference from a pair of signals. As such, the univariate implementation of SSA is not suitable; the multivariate case must be applied.

2.2 Multichannel Singular Spectrum Analysis

Multichannel singular spectrum analysis (M-SSA) expands on the previously discussed SSA technique in order to simultaneously decompose several time series. This method allows for common components to be identified using spatial and temporal similarities between the input signals (Gruszczynska et al., 2019). These common components are represented by a set of empirical bases, which can be used to isolate physically meaningful elements within a set of signals.

Practically, M-SSA can be implemented through the decomposition of a set of signals into their principal components, followed by reconstruction of the desired signal components (Groth & Ghil, 2011). Although this manuscript aims to utilize only two input signals by applying M-SSA component-wise to vector magnetic field data captured by two magnetometers, it generalizes to an arbitrary number of sensor measurements. The

specific steps required to realize this algorithm for a set of M one-dimensional input signals are as follows:

1. **Embedding.** Each input signal, x_m, is first embedded within a trajectory matrix, $\mathbf{X}_m$. This procedure can be viewed as generating a set of matrices whose columns correspond to a sliding window of length L applied to each input signal. These trajectory matrices can be written as

$$\mathbf{X}_m = \begin{bmatrix} x_m(1) & x_m(2) & \dots & x_m(K) \\ x_m(2) & x_m(3) & \dots & x_m(K+1) \\ \vdots & \vdots & & \vdots \\ x_m(L) & x_m(L+1) & \dots & x_m(N) \end{bmatrix} \quad \forall \ m \in \{1, \dots, M\}. \tag{1}$$

   The dimensions of the trajectory matrix are $L \times K$, where $K = (N - L + 1)$ for a signal of length N.

   Next, these matrices are concatenated together to form the full augmented trajectory matrix, $\mathbf{X}$. This can be written as

$$\mathbf{X} = \begin{bmatrix} \mathbf{X}_1 \\ \mathbf{X}_2 \\ \vdots \\ \mathbf{X}_M \end{bmatrix}. \tag{2}$$

   This full augmented trajectory matrix (with LM rows and K columns) contains information about how each of the input signals relates to one another on the scale of the window length. This information is leveraged in the subsequent steps in order to determine spatio-temporal relationships across the input signals.

2. **Eigendecomposition of Lag-Covariance Matrix.** The next step in the M-SSA procedure is to compute the lag-covariance matrix associated with $\mathbf{X}$. This symmetric $LM \times LM$ matrix is defined as

$$\mathbf{C} = \frac{1}{K}\mathbf{X}\mathbf{X}^T. \tag{3}$$

   The eigenvalues (λ_i) and associated eigenvectors (V_i) of the lag-covariance matrix are then extracted by performing eigendecomposition on $\mathbf{C}$. Mathematically, this decomposition is described via

$$\mathbf{C} = \mathbf{V}\mathbf{\Lambda}\mathbf{V}^{-1}, \tag{4}$$

where the columns of $\mathbf{V}$ are the eigenvectors V_i and the diagonal elements of $\mathbf{\Lambda}$ are the eigenvalues λ_i. It is important to note that, due to the augmented nature of the lag-covariance matrix, the calculated eigenvectors will be of length LM, where each consecutive section of length L is the basis for the m-th input signal.

3. **Projection.** The trajectory matrix can be projected onto the extracted basis as

$$\mathbf{P} = \mathbf{V}^T\mathbf{X}, \tag{5}$$

where the LM rows P_i correspond to the principal components of $\mathbf{X}$.

4. **Reconstruction.** The principal components, P_i, and the eigenvectors, V_i, can be used to reconstruct the related signal components via

$$\mathbf{R}_{m,i} = V_{m,i} \times P_i \;\; \forall \begin{array}{l} i \in \{1, \ldots, LM\} \\ m \in \{1, \ldots, M\} \end{array}, \tag{6}$$

where $V_{m,i}$ refers to the m-th consecutive L-length segment of the eigenvector V_i. Each matrix $\mathbf{R}_{m,i}$ can be reduced into its corresponding reconstructed component, $r_{m,i}$, by averaging along its skew diagonals. This process results in M sets of LM signals with length N that, when summed together, faithfully reconstruct the original M input signals:

$$x_m = \sum_{i=1}^{LM} r_{m,i} \;\; \forall \;\; i \in \{1, \ldots, LM\}. \tag{7}$$

This process of signal decomposition and reconstruction is demonstrated for a pair of synthetic signals in Fig. 4. Both signals, shown in Fig. 4a, contain the same near-DC trend and a fixed-frequency sinusoid with a different amplitude for each input. Additionally, Gaussian noise drawn from different distributions is applied to each input signal. It should also be noted that each signal was generated to be ten seconds long, sampled at a rate of 160 Hz. Additionally, the magnitude of the signals' trend, sinusoidal component, and additive noise was selected—in arbitrary units—to be proportionally representative of real in-situ data. This pair of signals was applied to the M-SSA algorithm with a window length of 200 samples. The impact of the window length parameter will be discussed in greater detail in Sec 2.4. Figure 4b shows the first five reconstructed components output by the M-SSA algorithm for both inputs. Brief inspection allows us to group these reconstructed components according to their contribution to either signal or noise: the first three components are related to the input signal (shown in blue) and the final two components contribute to the associated input noise (shown in red). All

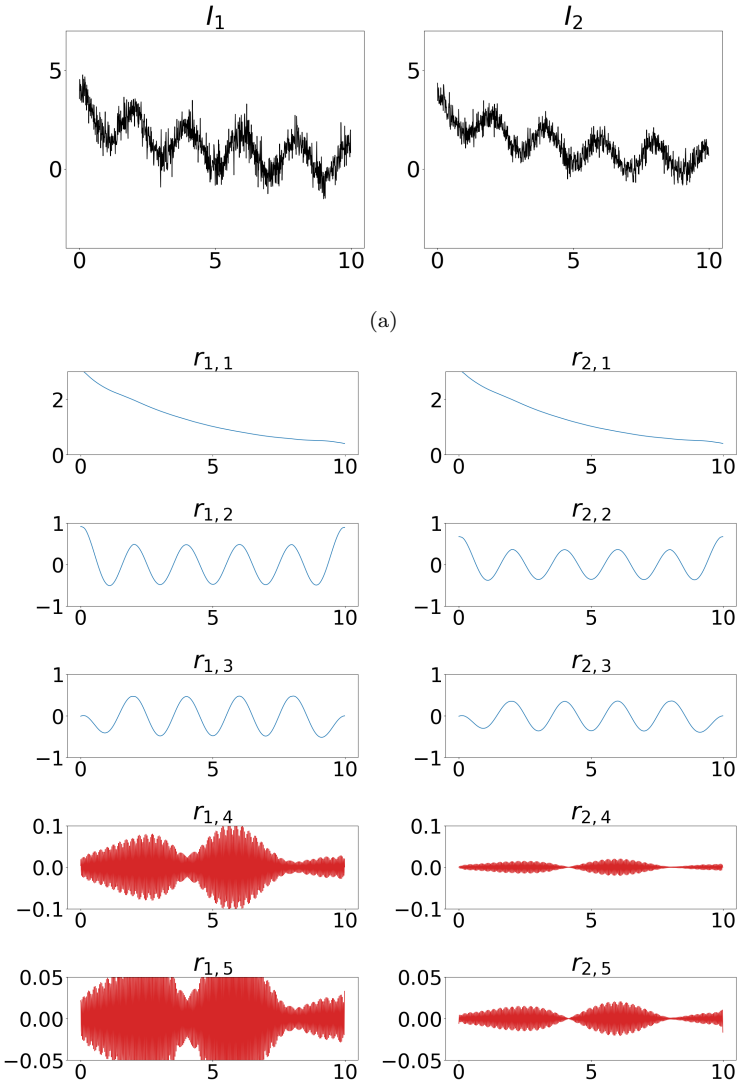

(a)

(b)

Figure 4: Multichannel singular spectrum analysis applied to a set of two synthetic input signals. (a) Input signals; (b) Reconstructed components output by the M-SSA algorithm, with inspection-based grouping indicated by blue for signal and red for interference.

reconstructed components after those illustrated here are also assumed to correspond to the additive Gaussian noise.

Figure 5 illustrates signal and noise reconstruction when this inspection-based grouping is applied and compares the results to the original input signal and noise. In this case, the signal components were reconstructed with a root-mean-square (RMS) error of 0.05 units and 0.04 units for the first and second inputs, respectively. This simple example

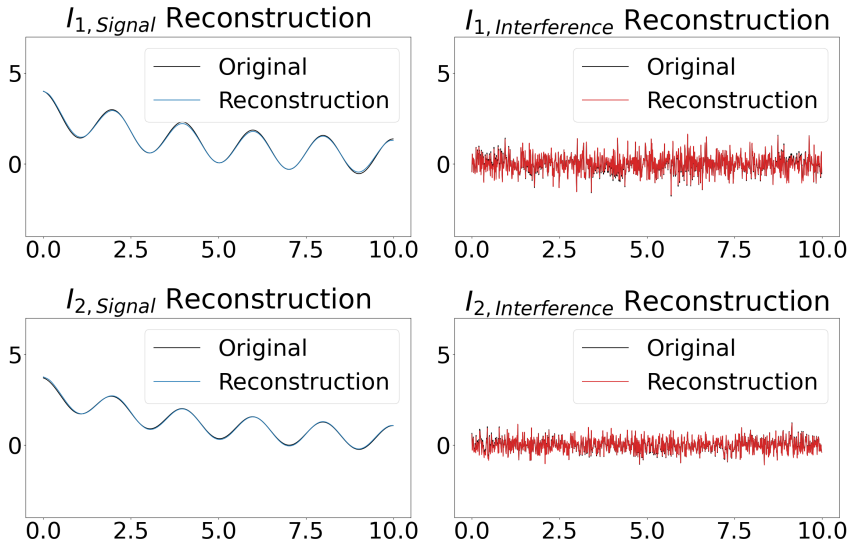

Figure 5: The result of inspection-based component grouping following signal decomposition with M-SSA. (left) Comparison of reconstructed and original signal; (right) Comparison of reconstructed and original interference.

illustrates that proper grouping of reconstructed components allows a user to isolate signals' trend, oscillatory modes, and signal interference with a high degree of accuracy.

2.3 Automatic Grouping of Reconstructed Components

As discussed in Sec. 1, the geophysical signals of interest observed by the two magnetometers onboard the Swarm-Echo spacecraft are assumed to be identical for each sensor. Additionally, the oscillatory magnetic interference caused by the spacecraft's reaction wheels is assumed to be in-phase when measured by the magnetometers. The complex multi-pole nature of the higher-order harmonics makes them difficult to remove using the simple difference between the two sensors (ΔB). As a result, the simple difference between the inboard and outboard sensors is a reasonable, but imperfect, approximation of the reaction wheel interference. This interference approximation can be defined mathematically, for the X-component of a magnetic vector, as

$$\hat{x}_{interference} = x_{inboard} - x_{outboard}. \tag{8}$$

It should be noted that this approximation can also be generated for the Y-component and Z-component in the same manner.

In order to algorithmically determine whether the reconstructed components calculated in Sec. 2.2 contribute to the reaction wheel interference, the correlation between this estimate and each component must be calculated. This is done using the Pearson correlation coefficient, which is generated by first calculating the correlation matrix for the magnetometer's x-axis via

$$\mathbf{F}_{ab} = \frac{\mathbf{C}_{ab}}{\sqrt{\mathbf{C}_{aa} * \mathbf{C}_{bb}}}. \tag{9}$$

Here, $\mathbf{C}_{ab}$ refers to the covariance matrix between the two input signals (e.g., $x_{inboard}$ and $x_{outboard}$) and $\mathbf{C}_{aa}$, $\mathbf{C}_{bb}$ refer to the covariance matrices for each input with itself. The identical elements of the skew diagonal for this symmetric 2×2 matrix ($\mathbf{F}_{ab}$) are the Pearson correlation coefficient between the input signals, ρ_{ab}.

Once calculated, the correlation between the interference approximation ($\hat{x}_{interference}$) and the reconstructed components ($r_{m,i}$) can be calculated. If the correlation is high, the decomposed component is similar to the noise approximation and can be grouped into a list of components representing magnetic interference. Mathematically, this thresholding and reconstruction operation is defined as

$$x_{interference,m} = \sum r_{m,i} \quad \forall \begin{array}{l} i \in \{1, \ldots, 2L \mid \rho_{ab} > \alpha\} \\ m \in \{1, 2\} \end{array}, \tag{10}$$

where α is a user-defined threshold value. This process can be repeated for each magnetometer axis and is demonstrated experimentally in Sec. 3. It should be noted that the correlation threshold parameter, α, is proportional to the confidence provided by the algorithm in classifying magnetic interference. For high values of α this technique will remove only the components that are most statistically similar to the interference approximation. For low values, more signals will be removed. As such, the correlation threshold parameter must be selected carefully when generating data products in order to balance false positive and false negative classification of signals.

2.4 Selection of Window Length

As the only user-defined parameter used in the M-SSA algorithm, window length (L) is clearly an important detail in the implementation of the method. In general, since the trajectory matrices $\mathbf{X}_m$—that are used to capture important information about the

input signals—are generated by sliding a window of length L over each input signal, window length must be selected such that the slowest oscillatory trend that must be seperated has a period defined inside a window. For example, if a sinusoidal trend at 10 Hz is to be isolated within the reconstructed components then the window length must be at least $\frac{1}{10}$ of a second. If this criteria is not satisfied, the sinusoidal trend cannot be successfully isolated by distinct reconstructed components. This is discussed in greater detail in Sec. 4.2. Additionally, the window length determines the absolute maximum number of sources that the proposed algorithm can theoretically detect. Given only two inputs (e.g., inboard and outboard measurements), the interference mitigation technique proposed in this manuscript can isolate only $2L$ independent noise sources.

3 Results

This section illustrates and analyzes the proposed method of spacecraft reaction wheel interference suppression.

3.1 Data

Section 2 provides an example of multichannel singular spectrum analysis (M-SSA) applied to a pair of synthetic signals. This section will apply the proposed method of simultaneous signal decomposition and automatic component selection to real geophysical measurements captured by e-POP's Magnetic Field Instrument (MGF) aboard the CASSIOPE/Swarm-Echo spacecraft (Wallis et al., 2015). The specific examples chosen for this manuscript were selected due to the occurrence of either interesting geophysical or interference phenomena. Geophysical phenomena such as field-aligned currents and Alfvén waves manifest primarily in the cross-track component; as such, this manuscript shows data from the spacecraft Y-component. However, the M-SSA algorithm and automatic component selection procedure performs equally well on all three axes. It should be noted that the physical data presented in this section—and elsewhere in this manuscript—has had it's near-DC baseline removed via a 20-second uniform filter (i.e., removing a 20-second running average from each sample). Additionally, it must be mentioned that this high-resolution magnetic data was captured at a rate of 160 samples per second.

The first event discussed in this section occurs on March 11, 2016, between 6:47:40 and 6:50:10 UTC (shown in Fig. 6a and Fig. 7a). During this time, the CASSIOPE/Swarm-

Echo spacecraft crossed a dynamic dual discrete arc aurora. Previous analysis of this event (Miles et al., 2019) demonstrated that, as the spacecraft transits magnetically conjugate to the aurora, it observes in-situ magnetic signatures of both a static field-aligned current (with $\sim$10$-$20 second period) and the nonstationary electrodynamics of reflected and interfereing Alfvèn waves (at $\sim$1$-$10 Hz) associated with the small-scale dynamic features observed in the auroral imaging.

The next event that is experimentally processed in this section occurs on March 16, 2016, between 4:50:00 and 5:10:00 UTC. The CASSIOPE/Swarm-Echo spacecraft performs a maneuver requiring significant reaction wheel dynamics during this interval, resulting in magnetic interference at simultaneous, variable frequencies. As can be seen in Fig. 8a, the reaction wheels begin at a rate of approximately 15 Hz and diverge during the course of the maneuver. The spacecraft's attitude control system then momentum dumps, allowing the reaction wheels to converge to the original $\sim$15 Hz rate.

3.2 Analysis

Although the synthetic data shown in Fig. 4 and Fig. 5 has a known ground truth and can therefore be analyzed directly using RMS accuracy, the data used in this section has no known ground truth (i.e., the true underlying geophysical signal is not known a priori). As such, in order to analyze the performance of the proposed method it is first necessary to define a metric that describes the reduction in magnetic interference from the spacecraft on real magnetometer measurements. In this section, numerical results are reported for the same ten second section of data in both the original measurement and the corrected measurement. Each subsequent second of data is linearly detrended based on the trend calculated using the original measurement. Then, the root-mean-square (RMS) value is calculated as

$$x_{m,RMS} = \sqrt{\frac{x_m(1)^2 + x_m(2)^2 + \ldots x_m(n)^2}{n}}.$$

Finally, the average RMS value for the ten subsequent assessments is calculated and reported as

$$\overline{x_{RMS}} = \frac{\sum_{m=1}^{10} x_{m,RMS}}{10}.$$

Since only intervals with near-constant background field are selected when performing the analysis, this metric provides a reasonable approximation of the performance of the magnetic interference suppression technique proposed in this manuscript.

3.3 Experiments

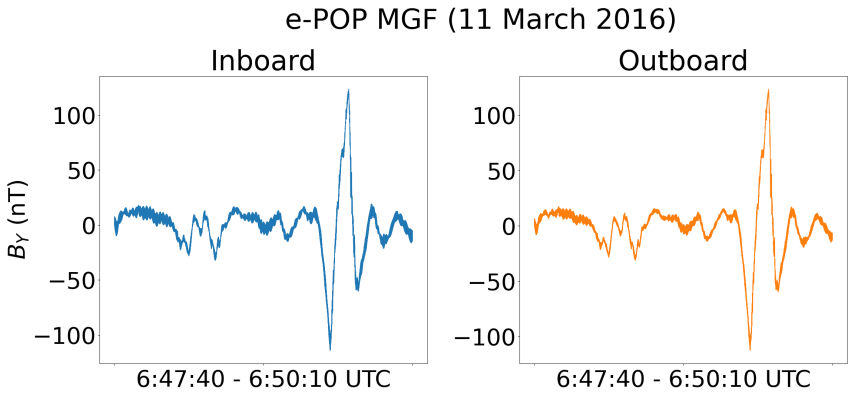

(a)

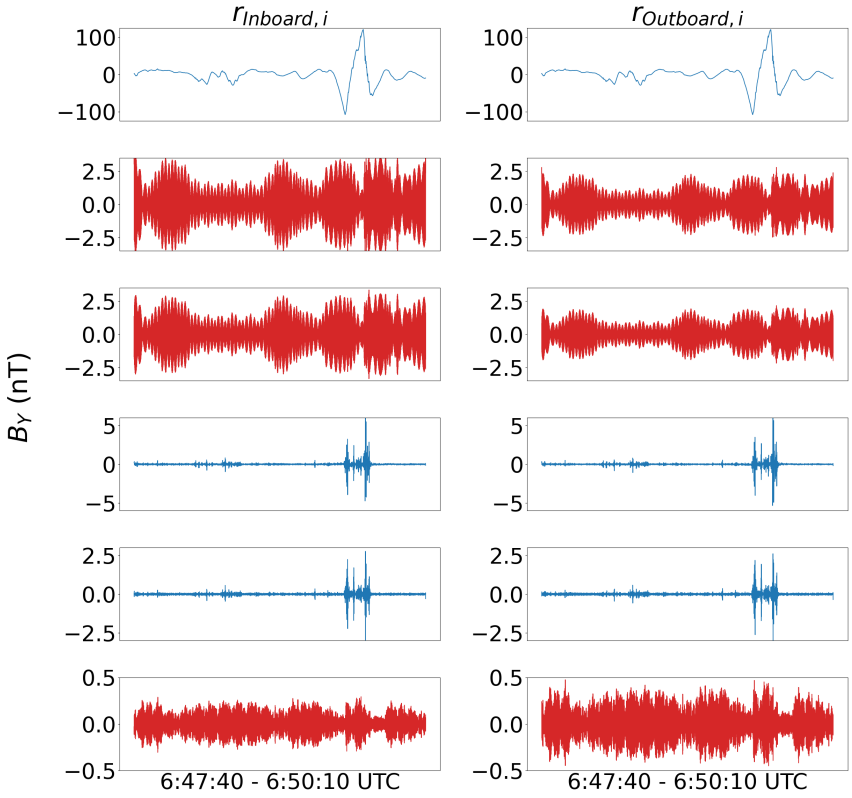

(b)

Figure 6: Multichannel singular spectrum analysis applied to the inboard and outboard magnetic field data captured by MGF on March 11, 2016 between 6:47:40 and 6:50:10 UTC. (a) Detrended time series for the inboard (left) and outboard (right) magnetometers; (b) Inboard (left) and outboard (right) reconstructed components output by the M-SSA algorithm with red indicating automatically identified interference components.

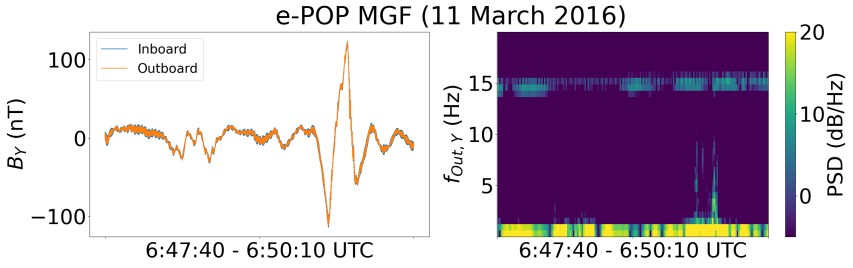

(a)

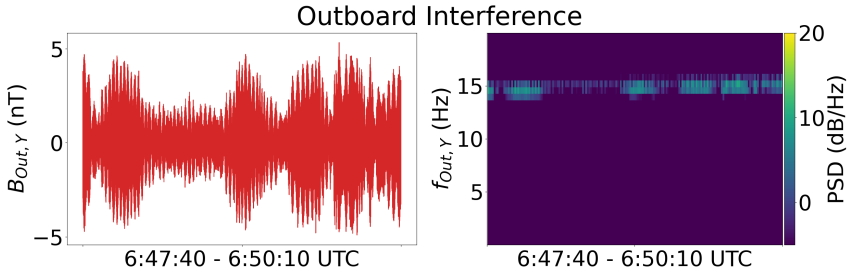

(b)

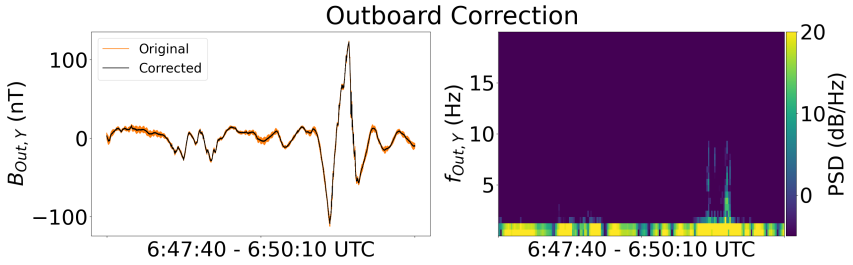

(c)

Figure 7: The proposed method of decomposition and component identification applied to the inboard and outboard magnetic field data captured by MGF on March 11, 2016 between 6:47:40 and 6:50:10 UTC. (a) Detrended time series and associated spectral content; (b) Reaction wheel interference estimate and associated spectrum; (c) Estimate of geophysical magnetic signal and associated spectrum.

The first experiment shown highlights the ability of multichannel singular spectrum analysis (M-SSA) to successfully decompose real magnetometer data into physically meaningful components that can be automatically grouped using the technique described in Sec. 2.3. Figure 6 illustrates the results of M-SSA applied to a pair of magnetometer measurements containing previously identified field-aligned currents and Alfvénic activity (Miles et al., 2019). The inboard and outboard magnetometer measurements are illustrated in

Fig. 6a. These signals were used as inputs to the M-SSA algorithm with a window size of 20 samples. The resultant reconstructed components are shown in Fig. 6b for the inboard and outboard sensors. The color coding corresponds to the output of the automatic component selection procedure: reconstructed components in red are those that were highly correlated to the noise estimate given by the interference approximation defined in Eqn. 8; components in blue are those that were not highly correlated. For the experiments in this manuscript a correlation threshold value of 0.05 was used (i.e., $\alpha = 0.05$ in Eqn. 10). This value was determined experimentally by the authors through trial and error: values higher than this tended to provide a less aggressive reduction in interference; values lower than this were often too aggressive and removed too much of the magnetic field measured by the sensors. Intriguingly, the reconstructed components in rows 4 and 5 of Fig. 6b appear to have blindly reconstructed—with no input from physics-based models—a signal morphologically similar to the Alfvén wave activity that was identified via band-pass filtering in Miles et al. (2019). The potential implications of this are discussed further in Sec. 4.4.

Once automatic grouping is performed the total interference term can be generated through the summation defined in Eqn. 10. This interference can be directly removed from the input time series via simple subtraction. The results of this process are illustrated in Fig. 7. Figure 7a provides the original inboard and outboard measurements (left) and the spectral content associated with the outboard sensor (right). The total isolated interference signal and associated frequency spectrum, for the outboard measurement, are illustrated in Fig. 7b. Figure 7c illustrate the resulting geophysical signal and associated frequency spectrum for the outboard sensor. It can be seen that a significant reduction in oscillatory magnetic interference is provided by the proposed technique. Further, this reduction can be analyzed numerically via the metric discussed in Sec. 3.2. For the section of data (with near-constant background field) between 6:48:00 and 6:48:10 UTC, the average one-second RMS value of the uncorrected outboard sensor is 1.90 nT. Following the correction procedure, the average one-second RMS value for the outboard sensor during the same time period was 0.21 nT (89.0% reduction in average RMS value).

The next experiment in this section illustrates the ability of the proposed method to isolate and remove presumed magnetic interference with a wide, variable frequency bandwidth. Figure 8 demonstrates the results of the method when applied to a section data where the reaction wheels were varying in speed. The inboard and outboard mag-

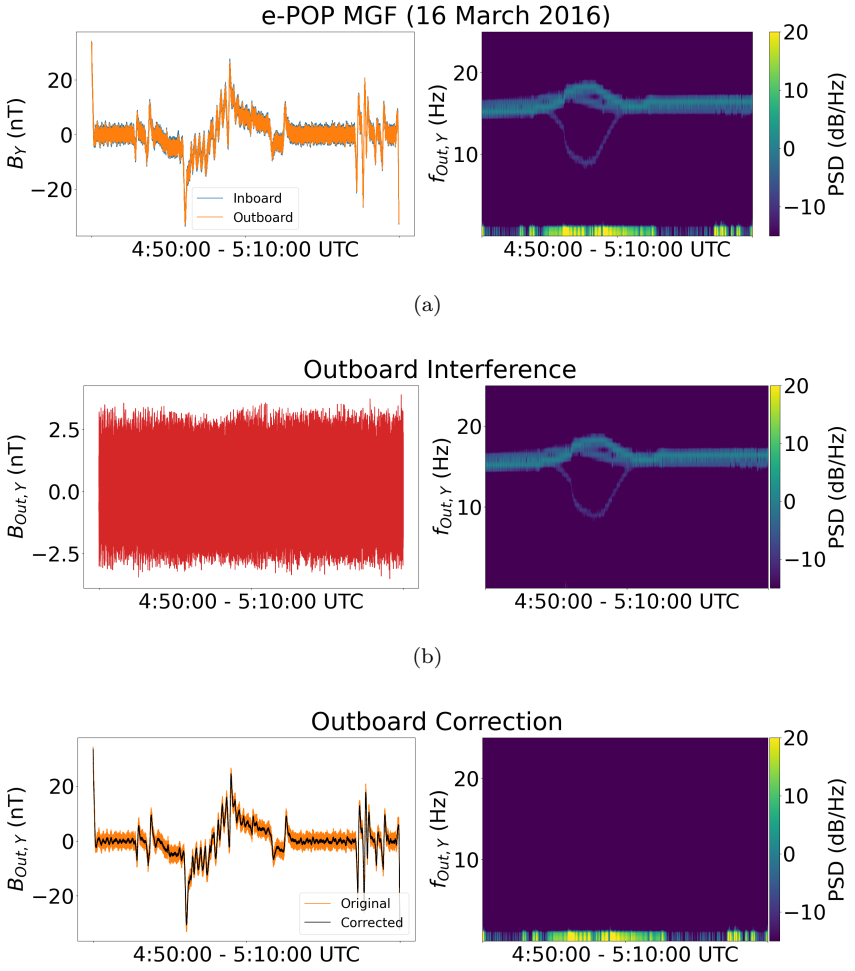

Figure 8: The proposed method of decomposition and component identification applied to the inboard and outboard magnetic field data captured by MGF on March 16, 2016 between 4:50:00 and 5:10:00 UTC. (a) Detrended time series and associated spectral content; (b) Reaction wheel interference estimate and associated spectrum; (d) Estimate of geophysical magnetic signal and associated spectrum.

netometer time-series measurements and associated outboard spectral content for this time period are shown in Fig. 8a. It can be seen that the frequency spectrum associated with the reaction wheel interference varies between approximately 10 and 20 Hz in this 20-minute interval. These two time series were used as the input to the M-SSA algorithm with a window size of 40 samples; the window length was increased, here, compared to previous experiment due to the decrease in minimum frequency that must be isolated.

Figure 8b shows the isolated outboard interference signal and frequency spectrum, generated through the automatic component grouping procedure described in Sec. 2. Figure 8c shows the corrected outboard signal, calculated by simply subtracting the isolated interference from the original input signal. Numerically, the reduction in interference is analyzed using the time period from 4:50:20 to 4:50:30 UTC, selected for its near-constant background field. The average one-second RMS value for the uncorrected outboard sensor in this interval is 1.23 nT. Following the correction process this value is reduced to 0.14 nT (88.3% reduction in average RMS value).

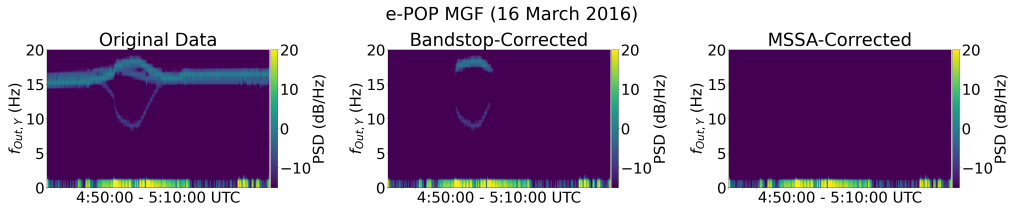

Figure 9: The proposed method of interference mitigation compared to a hand-tuned filter applied to magnetic field data captured by MGF on March 16, 2016 between 4:50:00 and 5:10:00 UTC. (left) Spectrogram illustrating the frequency spectrum of this interval; (middle) Spectrogram following the application of a bandstop filter between 12 and 17 Hz; (right) Spectrogram following the application of the interference mitigation technique proposed in this manuscript.

Figure 9 compares the result shown in Fig. 8, generated using the M-SSA-based technique proposed in this manuscript, to the output of a hand-tuned bandstop filter. Specifically, the original 20-minute interval's spectrum (left) is compared to the data's spectrum following the application of a bandstop filter (center). The filter used was a sixth-order Butterworth implementation with cutoff frequencies at 12 and 17 Hz. These parameters were selected in order to provide a more reasonable frequency-rejection region than that illustrated in Fig. 3 while still removing the dominant reaction wheel interference frequency band. It can be seen that although the bandstop filter is able to mitigate the majority of the reaction wheel interference, it fails to remove the interference signal when the reaction wheel rates diverge. However, the spectrum resulting from the application of the proposed technique (right) shows that it is capable of isolating and

removing the dynamic interference signal—without a change of parameters or knowledge of the spacecraft subsystems—regardless of the divergence in reaction wheel rates.

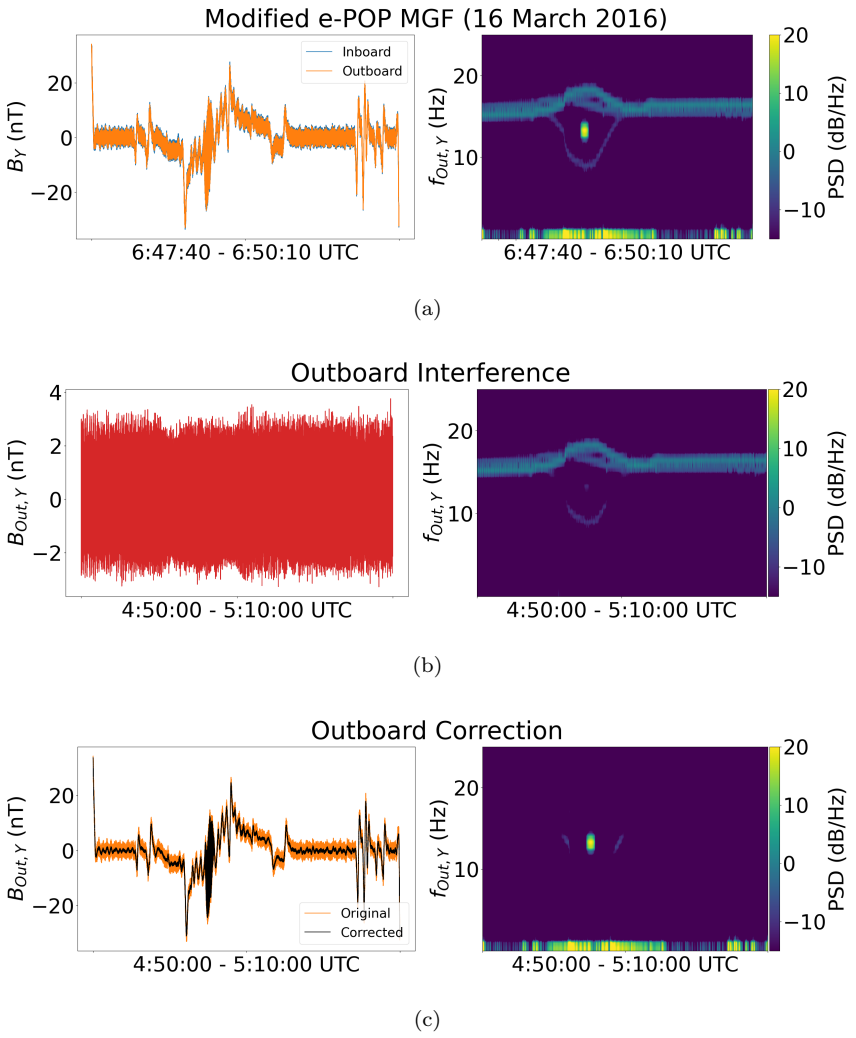

Figure 10: The proposed method of decomposition and component identification applied to a modified inboard and outboard measurement from MGF. The time series, from 4:50:00 to 5:10:00 UTC, was modified with a synthetic Alfvén wave. (a) Inboard and outboard measurements and associated outboard spectral content; (b) Estimated outboard interference and associated spectrum; (c) Outboard correction and spectral content.

The final experiment in this section expands on the previous experiments to highlight the ability of the proposed method to automatically isolate and remove magnetic interference without discarding signal components in the same bandwidth. Figure 10a shows the data used in this experiment: in this case, the same inboard and outboard mea-

surements shown in Fig. 8, now modified with a simple synthetic Alfvén wave at 13 Hz injected at 4:57:15 UTC. This wave frequency was selected due to the difficulty associated with removing reaction wheel interference while preserving important geophysical signals using traditional lowpass or bandpass filtering techniques. These two measurements were input to the M-SSA algorithm with a window length of 60 samples. Figure 10b illustrates the estimated reaction wheel interference, generated by automatically grouping the reconstructed components output by the M-SSA algorithm. Figure 10c gives the result of the proposed method of interference mitigation for the outboard sensor. It can be seen that the synthetic signal component is preserved while heavily attenuating the magnetic interference caused by the spacecraft's reaction wheels. The section of data from 4:50:20 to 4:50:30 UTC—with near-constant background field—is once again analyzed in this experiment. The original, unprocessed data has an average one-second RMS value of 1.23 nT, as before. Following the interference mitigation process described in this manuscript, the average one-second RMS value of the outboard sensor is reduced to 0.17 nT, resulting in an 86.4% reduction in RMS value that can be attributed to attenuation of stray magnetic field.

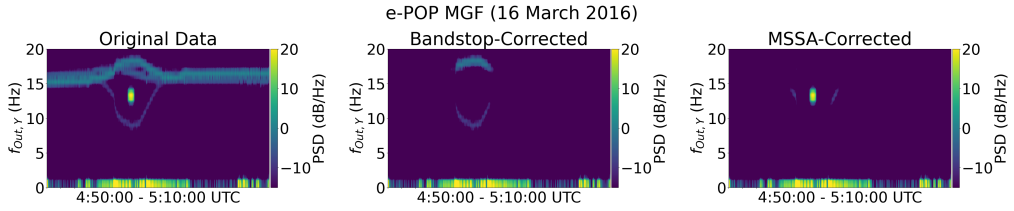

Figure 11: The proposed method of interference mitigation compared to a hand-tuned filter applied to modified magnetic field data captured by MGF on March 16, 2016 between 4:50:00 and 5:10:00 UTC. (left) Spectrogram illustrating the frequency spectrum of this interval; (middle) Spectrogram following the application of a bandstop filter between 12 and 17 Hz; (right) Spectrogram following the application of the interference mitigation technique proposed in this manuscript.

Figure 11 compares these results (shown in Fig. 10) to the output of the same hand-tuned bandstop filter used in Fig. 9. The original 20-minute interval of data, with a synthetic Alfvén wave at 13 Hz injected during the period where the reaction wheel rates diverge, has spectrum illustrated in the leftmost panel. The center panel of Fig. 11 il-

lustrates the spectrum after the application of a bandstop filter with cutoff frequencies at 12 and 17 Hz, respectively. Note that this bandstop implementation is capable of mitigating the dominant reaction wheel signature, but removes the synthetic signal of interest in the process. The rightmost panel of Fig. 11 provides the same spectrum as shown in Fig. 9, which results from the application of the M-SSA-based interference mitigation scheme proposed in this manuscript. This technique removes more of the reaction wheel interference than the simple bandstop filter, but most importantly preserves the synthetic signal of interest, regardless of the highly dynamic interference surrounding it in both time and frequency.

4 Discussion and Future Work

This manuscript has demonstrated a novel technique for the reduction of spacecraft-based magnetic interference in applications where multiple magnetometers are deployed. Several experiments in Sec. 3 demonstrate the ability of this method to resolve geophysical phenomenon and isolate a wide, variable interference bandwidth. However, it is necessary to discuss some of this method's potential limitations and highlight avenues for future work.

4.1 Spectral Overlap

One limitation of the proposed method is that, like many model-free algorithms, signal components cannot be effectively separated from the associated interference component if they have simultaneous time and frequency spectrum overlap (Ghaderi et al., 2011; Davies & James, 2007). Several methods have been proposed that are capable of separating signals that exhibit simultaneous time-frequency overlap (Li et al., 2009; Parsons, 1976; Virtanen & Klapuri, 2001; Al-Oudatallah et al., 2017; Sun et al., 2011), but these often require constraints or specific statistical properties to hold for the input data; these constraints are not required for our proposed algorithm, and can not generally be assumed to hold for the magnetic field data captured by the gradiometer onboard CASSIOPE/Swarm-Echo. Figure 12 provides a synthesized example of spectral overlap between a signal of interest and the underlying magnetic interference. In this case, an interval of e-POP/Swarm-Echo data from March 16, 2016 with near-constant background field is used to represent the interference. The reaction wheels manifest at a frequency of approximately 15 Hz during this time interval. A synthetic chirp wave with constant amplitude and fre-

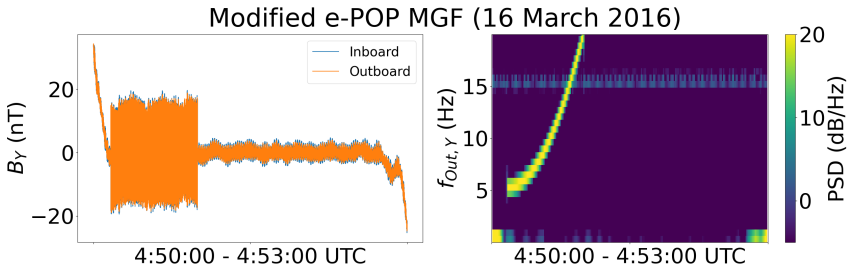

(a)

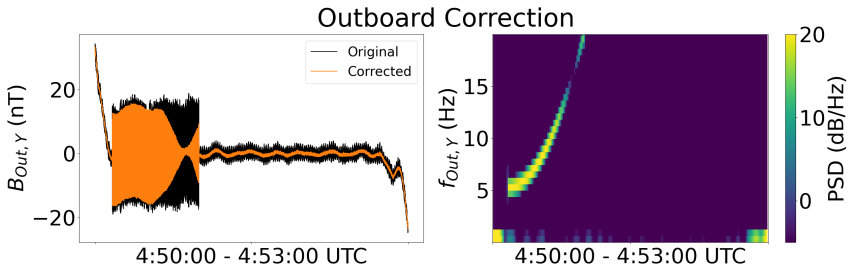

(b)

Figure 12: Multichannel singular spectrum analysis applied to magnetometer data from the MGF instrument modified with a synthetic chirped waveform. (a) Inboard and outboard signals input to the M-SSA algorithm with associated outboard spectral content; (b) Corrected outboard signal and associated spectrum.

quencies between five and 25 Hz are added to the data to simulate a geophysical signal of interest. Figure 12a illustrates the inboard and outboard signals (left) and the spectral content associated with the outboard magnetometer (right). These signals were used as inputs to the M-SSA algorithm with a window length of 20 samples. The outboard correction results, following the automatic component selection procedure and subsequent interference removal, are shown in Fig. 12b. Although the proposed method is able to significantly attenuate supposed wheel interference, some of the signal of interest is also discarded, but only where the simulated signal overlaps the instantaneous frequency of the reaction wheels. The majority of the magnetic data captured by the e-POP/Swarm-Echo spacecraft has nominal reaction wheel rates of approximately 15 Hz, but these rates can vary significantly, even throughout a single 90-minute orbit. As a result, the proposed method still shows improvement when compared to a comparable bandstop interference mitigation approach (such as that shown in Fig. 9), which would require a large frequency-

rejection band in order to handle all possible reaction wheel frequencies for that interval, potentially reducing the ability to observe interesting geophysical phenomena.

4.2 Window Length

As discussed in Sec. 2.4, selection of an appropriate window length is critical to the separation of signal components when utilizing the M-SSA technique. Although the minimum window length required to isolate oscillatory trends is simply the same as the period of the slowest oscillation, adjusting window length above that value can impact the separability of signals in cases of near-overlap in the spectral domain (Harmouche et al., 2017). Thus, it can sometimes be beneficial to use larger window sizes than what is strictly necessary when implementing the method described in this manuscript. However, this can have the negative impact of reducing the statistical significance of each reconstructed component ($r_{m,i}$). Increasing window length also exponentially increases the computational complexity of the M-SSA algorithm (Golyandina et al., 2013a). As a result, users must carefully balance computational costs, separability, and statistical significance when applying the proposed method.

4.3 Component Selection via Eigenvector Pairs

Several of the experiments in this paper highlight an important characteristic of the singular spectrum analysis decomposition technique: a sinusoidal input will typically result in *two* sinusoidal or approximately sinusoidal eigenvectors with nearly identical eigenvalues (Golyandina et al., 2013b; Hassani, 2007). Further, the pair of eigenvectors will be phase-shifted by $\sim\frac{\pi}{2}$ due to the necessary condition of orthogonality. The authors of this manuscript believe that this unique relationship may be useful in defining additional processing steps in the automatic grouping of reconstructed components. For example, if any two eigenvectors have a high degree of cross-correlation at a lag of $\sim\frac{\pi}{2}$, or any two eigenvalues are nearly the same, they may be suitable for classification as reaction wheel interference. Although interesting, this additional step is out of scope for this manuscript and is left as a potential avenue for future work.

4.4 Geophysical Signal Detection with Machine Learning

The significant recent advances in machine learning tools have allowed for their adoption in heliophysics and related fields (e.g., Galvez et al. (2019); Nita et al. (2020)). The M-SSA technique utilized in this manuscript provides a possible avenue for future work involving machine learning techniques. This manuscript has shown that M-SSA is capable of decomposing potentially noisy signals into physically meaningful components. A machine learning network, trained on hand-labeled data and applied following this decomposition, could allow a tag to be automatically applied to each of the reconstructed components in order to indicate the possible inclusion of interesting geophysical phenomena such as field-aligned currents and Alfvénic activity. This would allow for the massive quantities of data captured during the lifespan of a spacecraft to be classified automatically; important scientific phenomena could be identified and analyzed with less scrutiny of scientifically benign data.

For example, Miles et al. (2019) used a hand-tuned band-pass filter to identify Alfvénic power between 0.2 and 4 Hz occurring co-incident with magnetically conjugate dynamic discrete arc aurora. This frequency range was selected based on local plasma conditions and the artificial upper frequency constraint imposed by the reaction wheels. Figure 13 compares the outboard signal extracted by a comparable band-pass filter between 0.2 and 4.0 Hz (shown in Fig. 13a) to the signal extracted via the simple summation of rows 4 and 5 from Fig. 6b (shown in Fig. 13b). It can be seen that the sum of the two M-SSA reconstructed components captures activity during the same intervals as the bandpass filter, but is unable to capture the significant low-frequency power that was resolved following the application of the bandpass filter. This is a result of the relatively low window length (20 samples) used in this experiment. In order to capture the 0.2 Hz trends present following the application of a 0.2 to 4.0 Hz bandpass filter, a window length of 800 would be required (i.e., 160 samples/sec $\div$ 0.2 Hz). This increases the computational complexity of the M-SSA algorithm significantly, and is unnecessary for the correct characterization and classification of reaction wheel interference for this sample of data. However, the authors believe that the signal present in Fig. 13b may be sufficient in the identification of geophysical waveforms. Future work will examine the potential of training a neural net to identify Alfvénic activity based on the composed components rather than the raw magnetic time series. This may allow for robust, automated identification of intervals with significant wave power without human intervention.

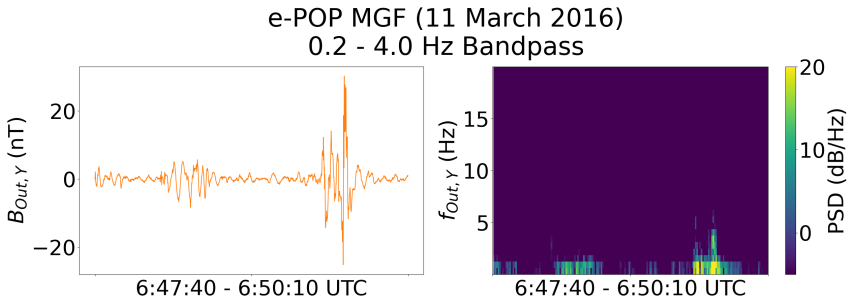

(a)

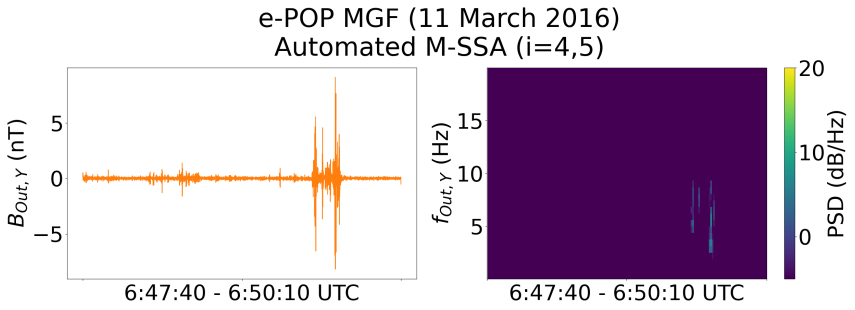

(b)

Figure 13: Previously identified Alfvénic activity using a hand-tuned bandpass filter compared to the multichannel singular spectrum analysis technique with manually selected reconstructed components. (a) Bandpass filter between 0.2 and 4.0 Hz applied to the outboard magnetic field measurements; (b) Manual component selection corresponding to the manually selected, morphologically similar components output by the multichannel singular spectrum analysis technique.

4.5 Automation for Large Datasets

The CASSIOPE/Swarm-Echo spacecraft makes a full orbit every $\sim$ 90 minutes, although the MGF observations can be shorter than this. In the early mission, from 2013 to 2016, these observations were limited to higher latitudes when auroral activity was detected, with an occasional equator crossing for instrument calibration purposes. Although the number and length of MGF observations increased each year, a maximum of approximately 80% coverage in each 24-hour period was reached in 2019 due to power constraints on the spacecraft. The observations captured often include discontinuities from packets dropped during uplink, or clipped samples, which are challenging for algorithms which assume continuous finite samples. For the operational use of this algo-

rithm, the authors are actively developing software which segments these observations into shorter observing intervals which are processed independently. This allows the discontinuities to be avoided and the segmented, continuous magnetic field data is then passed into the proposed algorithm. This automatic segmentation procedure has the added benefit of increasing computational efficiency as the M-SSA algorithm has complexity that scales with the length of the interval under analysis, on the order of $\sim \mathcal{O}(N^3)$ for signals with length N (Golyandina et al., 2013c). Although further details of such a large-scale and robust software suite are outside the scope of this manuscript, the authors have identified one of the MGF observations that captures an entire orbit of the CASSIOPE/Swarm-Echo spacecraft during the early mission in order to illustrate the performance of the proposed method on larger data intervals, as well as some of the issues that will need to be handled in operational deployment.

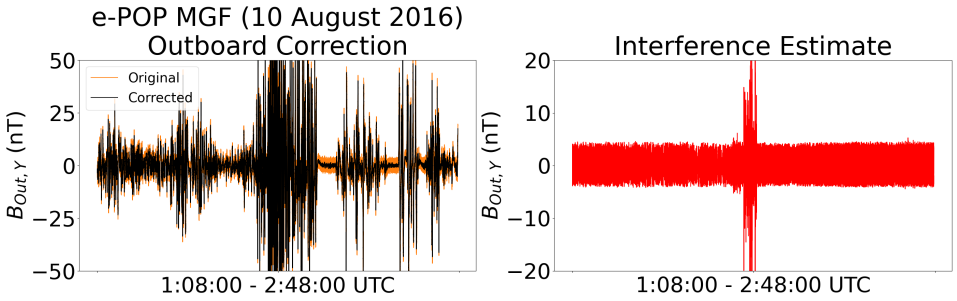

(a) (b)

Figure 14: The proposed method applied to an entire $\sim$ 90-minute orbit of MGF instrument data. (a) Illustration of correction applied to the outboard sensor; (b) Estimated interference.

Figure 14 illustrates the proposed interference mitigation technique applied to a $\sim$ 90 minute observation from the e-POP MGF on August 10, 2016 from 1:08 to 2:48 UTC. Figure 14a shows the original outboard sensor's magnetic field measurement in orange, with the automatic M-SSA-based correction in black. Figure 14b is the interference estimated by the proposed method. It should be noted that the large amplitude spike in Fig. 14b, at approximately 1:58 UTC, represents the point in orbit where CASSIOPE/Swarm-Echo leaves eclipse. As mentioned in Sec. 1, the increased current across the solar panels, combined with the currents caused by various spacecraft subsystems cycling power,

induce a large time-varying stray field on the magnetometers that is typically difficult to characterize. Although characterization and removal of all types of magnetic interference present onboard a spacecraft is outside the scope of this manuscript, this is indicative of the potential for this method to extend beyond the mitigation of reaction wheel interference and remove interference from a variety of time-varying onboard sources.

5 Conclusion

This manuscript has presented a novel method for the isolation and removal of magnetic interference in systems where two or more magnetometers are present. Specifically, an automatic component selection procedure is employed, alongside the multivariate extension of singular spectrum analysis, in order to increase the fidelity of magnetometer data in the presence of stray field from magnetically noisy spacecraft. Experimental results demonstrated the effectiveness of this technique on synthetic data and real gradiometric magnetometer data from the CASSIOPE/Swarm-Echo mission. For example, on a section of data from this mission with near-constant background field, the proposed method achieved a 89.0% reduction in average RMS value attributed to magnetic interference mitigation. Further, the authors have highlighted several potential limitations and avenues for future work in the application of this technique.

Open Research

The CASSIOPE/Swarm-Echo e-POP data used in this manuscript is publicly available at `https://epop-data.phys.ucalgary.ca/`.

Acknowledgments

The CASSIOPE/Swarm-Echo mission is supported by the European Space Agency's Third Party Mission Program. This work was supported in part by the US Air Force Office of Scientific Research (FA9550-21-1-0206). The authors thank Ananya Sen Gupta for her thoughtful insights and careful proofreading of this manuscript.

References

Acuña, M., Scearce, C., Seek, J., & Scheifele, J. (1978). *The magsat vector magnetometer: A precision fluxgate magnetometer for the measurement of the geomagnetic field* (Tech. Rep.).

Al-Oudatallah, J., Abboud, F., Khoury, M., & Ibrahim, H. (2017). Overlapping signal separation method using superresolution technique based on experimental echo shape. *Advances in Acoustics and Vibration*, *2017*.

Broadfoot, R. M., Miles, D. M., Holley, W., & Howarth, A. D. (2022). In-situ calibration of the swarm-echo magnetometers. *EGUsphere*, 1–17.

Broomhead, D. S., & King, G. P. (1986). Extracting qualitative dynamics from experimental data. *Physica D: Nonlinear Phenomena*, *20*(2-3), 217–236.

Chen, Q., van Dam, T., Sneeuw, N., Collilieux, X., Weigelt, M., & Rebischung, P. (2013). Singular spectrum analysis for modeling seasonal signals from gps time series. *Journal of Geodynamics*, *72*, 25–35.

Davies, M. E., & James, C. J. (2007). Source separation using single channel ica. *Signal Processing*, *87*(8), 1819–1832.

Galvez, R., Fouhey, D. F., Jin, M., Szenicer, A., Muñoz-Jaramillo, A., Cheung, M. C., ... others (2019). A machine-learning data set prepared from the nasa solar dynamics observatory mission. *The Astrophysical Journal Supplement Series*, *242*(1), 7.

Ghaderi, F., Mohseni, H. R., & Sanei, S. (2011). Localizing heart sounds in respiratory signals using singular spectrum analysis. *IEEE Transactions on Biomedical Engineering*, *58*(12), 3360–3367.

Golyandina, N., Korobeynikov, A., Shlemov, A., & Usevich, K. (2013a). Multivariate and 2d extensions of singular spectrum analysis with the rssa package. *arXiv preprint arXiv:1309.5050*.

Golyandina, N., Korobeynikov, A., Shlemov, A., & Usevich, K. (2013b). Multivariate and 2d extensions of singular spectrum analysis with the rssa package. *arXiv preprint arXiv:1309.5050*.

Golyandina, N., Korobeynikov, A., Shlemov, A., & Usevich, K. (2013c). Multivariate and 2d extensions of singular spectrum analysis with the rssa package. *arXiv preprint arXiv:1309.5050*.

Groth, A., & Ghil, M. (2011). Multivariate singular spectrum analysis and the road to phase synchronization. *Physical Review E*, *84*(3), 036206.

Gruszczynska, M., Rosat, S., Klos, A., Gruszczynski, M., & Bogusz, J. (2019). Multichannel singular spectrum analysis in the estimates of common environmental effects affecting gps observations. In *Geodynamics and earth tides observations*

from global to micro scale (pp. 211–228). Springer.

Harmouche, J., Fourer, D., Auger, F., Borgnat, P., & Flandrin, P. (2017). The sliding singular spectrum analysis: A data-driven nonstationary signal decomposition tool. *IEEE Transactions on Signal Processing*, *66*(1), 251–263.

Hassani, H. (2007). Singular spectrum analysis: methodology and comparison.

Hassani, H., & Zhigljavsky, A. (2009). Singular spectrum analysis: methodology and application to economics data. *Journal of Systems Science and Complexity*, *22*(3), 372–394.

Imajo, S., Nosé, M., Aida, M., Matsumoto, H., Higashio, N., Tokunaga, T., & Matsuoka, A. (2021). Signal and noise separation from satellite magnetic field data through independent component analysis: prospect of magnetic measurements without boom and noise source information. *Journal of Geophysical Research: Space Physics*, *126*(5), e2020JA028790.

Kepko, L., Clagett, C., Santos, L., Azimi, B., Berry, D., Bonalsky, T., ... others (2017). Dellingr: Nasa goddard space flight center's first 6u spacecraft.

Kletzing, C., Kurth, W., Acuna, M., MacDowall, R., Torbert, R., Averkamp, T., ... others (2013). The electric and magnetic field instrument suite and integrated science (emfisis) on rbsp. *Space Science Reviews*, *179*(1), 127–181.

Li, Y., Woodruff, J., & Wang, D. (2009). Monaural musical sound separation based on pitch and common amplitude modulation. *IEEE Transactions on Audio, Speech, and Language Processing*, *17*(7), 1361–1371.

Mann, I., Nokes, C., Cupido, C., Miles, D., Bruner, B., Elliott, D., ... others (2020). The experimental albertan satellite# 1 (ex-alta 1) cube-satellite mission. *Space Science Reviews*, *216*(5), 1–35.

Miles, D. M., Howarth, A. D., & Enno, G. A. (2019). In situ calibration of offsetting magnetometer feedback transients on the cassiope spacecraft. *Geoscientific Instrumentation, Methods and Data Systems*, *8*(2), 187–195.

Ness, N. F., Behannon, K. W., Lepping, R. P., & Schatten, K. H. (1971). Use of two magnetometers for magnetic field measurements on a spacecraft. *Journal of Geophysical Research*, *76*(16), 3564–3573.

Neubauer, F. (1975). Optimization of multimagnetometer systems on a spacecraft. *Journal of Geophysical Research*, *80*(22), 3235–3240.

Nita, G., Georgoulis, M., Kitiashvili, I., Sadykov, V., Camporeale, E., Kosovichev,

A., ... others (2020). Machine learning in heliophysics and space weather forecasting: a white paper of findings and recommendations. *arXiv preprint arXiv:2006.12224*.

Parsons, T. W. (1976). Separation of speech from interfering speech by means of harmonic selection. *The Journal of the Acoustical Society of America*, *60*(4), 911–918.

Pope, S., Zhang, T., Balikhin, M., Delva, M., Hvizdos, L., Kudela, K., & Dimmock, A. (2011). Exploring planetary magnetic environments using magnetically unclean spacecraft: a systems approach to vex mag data analysis. In *Annales geophysicae* (Vol. 29, pp. 639–647).

Russell, C., Anderson, B., Baumjohann, W., Bromund, K., Dearborn, D., Fischer, D., ... others (2016). The magnetospheric multiscale magnetometers. *Space Science Reviews*, *199*(1), 189–256.

Sen Gupta, A., & Miles, D. M. (2022). Autonomous reaction wheel magnetic signature detection against background noise in spacecrafts. *IEEE Sensors Letters (In Review)*.

Sheinker, A., & Moldwin, M. B. (2016). Adaptive interference cancelation using a pair of magnetometers. *IEEE Transactions on Aerospace and Electronic Systems*, *52*(1), 307–318.

Slavin, J. A., Le, G., Strangeway, R., Wang, Y., Boardsen, S., Moldwin, M., & Spence, H. E. (2008). Space technology 5 multi-point measurements of near-earth magnetic fields: Initial results. *Geophysical research letters*, *35*(2).

Sun, Y., Ridge, C., Del Rio, F., Shaka, A. J., & Xin, J. (2011). Postprocessing and sparse blind source separation of positive and partially overlapped data. *Signal Processing*, *91*(8), 1838–1851.

Vautard, R., & Ghil, M. (1989). Singular spectrum analysis in nonlinear dynamics, with applications to paleoclimatic time series. *Physica D: Nonlinear Phenomena*, *35*(3), 395–424.

Virtanen, T., & Klapuri, A. (2001). Separation of harmonic sounds using multipitch analysis and iterative parameter estimation. In *Proceedings of the 2001 ieee workshop on the applications of signal processing to audio and acoustics (cat. no. 01th8575)* (pp. 83–86).

Wallis, D., Miles, D., Narod, B., Bennest, J., Murphy, K., Mann, I., & Yau, A.

(2015). The cassiope/e-pop magnetic field instrument (mgf). *Space Science Reviews*, *189*(1), 27–39.

Yau, A., & James, H. (2015). Cassiope enhanced polar outflow probe (e-pop) mission overview. *Space Science Reviews*, *189*(1), 3–14.